



Facile route for the preparation of ordered intermetallic Pt₃Pb–PtPb core–shell nanoparticles and its enhanced activity for alkaline methanol and ethanol oxidation

Takao Gunji^a, Toyokazu Tanabe^a, Arockiam John Jeevagan^a, Sho Usui^a, Takashi Tsuda^a, Shingo Kaneko^b, Govindachetty Saravanan^c, Hideki Abe^{d,e}, Futoshi Matsumoto^{a,*}

^a Department of Material and Life Chemistry, Kanagawa University, 3-27-1, Rokkakubashi, Kanagawa-ku, Yokohama, Kanagawa 221-8686, Japan

^b Research Institute for Engineering, Kanagawa University, 3-27-1, Rokkakubashi, Kanagawa-ku, Yokohama, Kanagawa 221-8686, Japan

^c CSIR-National Environmental Engineering Research Institute (CSIR-NEERI), Nehru Marg, Nagpur 440020, India

^d National Institute for Materials Science (NIMS), 1-2-1 Sengen, Tsukuba, Ibaraki 305-0047, Japan

^e PRESTO, Japan Science and Technology Agency (JST), 4-1-8 Honcho, Kawaguchi, Saitama 332-0012, Japan

HIGHLIGHTS

- Pt₃Pb–PtPb core–shell NPs were prepared on carbon black at room temperature.
- The core–shell structure was characterized with XRD, XPS and TEM.
- The core–shell NPs showed higher activity for EtOH oxidation compared to PtPb.
- The relationship between the surface structure and the catalytic activity was evaluated.

ARTICLE INFO

Article history:

Received 10 July 2014

Received in revised form

14 September 2014

Accepted 30 September 2014

Available online 6 October 2014

Keywords:

Electrocatalysis

Ordered intermetallic compound

Core–shell structure

Ethanol oxidation

Fuel cell

ABSTRACT

Pt₃Pb(core)–PtPb(shell) intermetallic compound nanoparticles (NPs) were synthesized on carbon black (CB) by converting nanocrystalline Pt to an ordered intermetallic compound with the reduction of Pb ions. The Pt₃Pb–PtPb core–shell NPs were characterized by analyzing their crystal structures with powder X-ray diffraction (pXRD), hard X-ray photoemission spectroscopy (HX-PES), and transmission electron microscopy (TEM). The synthesized NPs exhibited enhanced catalytic activity and relatively stable cycle performance towards methanol (MeOH) and ethanol (EtOH) oxidation in an alkaline aqueous solution. The improved catalytic performance of the Pt₃Pb–PtPb core–shell NPs might be attributed to both the enhancement of EtOH dehydrogenation and the higher concentration of surface OH_{ads} at lower potential on the modified PtPb surface in the Pt₃Pb–PtPb core–shell NPs.

© 2014 Published by Elsevier B.V.

1. Introduction

In recent years, within the polymer electrolyte membrane fuel cell research field, enormous attention has been directed towards the development of direct fuel cells (DFCs) in which small organic molecule (SOM) liquid fuels, such as methanol (MeOH), ethanol (EtOH), and formic acid (FA), are used as fuels [1,2]. Among the main fuel molecules, EtOH is a promising alternative fuel because of its relatively low toxicity and high energy density and because it does not release carbon that was previously sequestered

underground as coal, petroleum, or natural gas into the atmosphere [3]. However, the full potential of DFCs has not been fulfilled due to the slow kinetics in the anode reactions [4]. It has been reported that the oxidation kinetics of organic fuels in acidic media exhibits slower kinetics than in alkaline environments due to catalyst poisoning by reaction intermediates [5]. One of the research and development challenges facing alkaline-type polymer electrolyte fuel cells using SOMs is the design of better alternatives to the Pt, Pd, and Pt–Ru alloys currently used as the anode catalysts [6,7]. To improve the electrocatalytic activity, Pt- and Pd-based alloy electrocatalysts have been investigated in alkaline media [8]. Although the aforementioned alloys are promising materials, there are problems associated with the use of disordered alloys (and alloys in general) as catalysts for fuel cell applications, including the surface

* Corresponding author. Fax: +81 45 413 9770.

E-mail address: fmatsumoto@kanagawa-u.ac.jp (F. Matsumoto).

segregation of metal atoms and the partial poisoning by CO due to insufficient quantities of the bimetallic elements on the surface.

Recently, a new approach that avoids the problems inherent in disordered alloy catalysts has been proposed for highly active electrocatalysts for fuel cell applications [9]. In contrast with disordered alloys, intermetallic compounds with definite compositions and structures, such as PtPb and PtBi, exhibit excellent electrocatalytic performance towards FA oxidation in acidic solutions in terms of onset potential and current density [10,11]. Abruña et al. have examined the FA, MeOH, and EtOH oxidation activities with a wide range of intermetallic compounds (PtPb, PtBi, and Pt₃Ti) in acidic media and found that the intermetallic compounds exhibit enhanced catalytic activity when compared with pure Pt [10,11]. In our previous study, we reported that PtPb and PtBi ordered intermetallic compounds exhibited higher electrocatalytic activity towards MeOH and EtOH oxidation in alkaline aqueous solutions than Pt, Pt–Ru alloy, and other Pt-based ordered intermetallic compounds [12]. In this paper, we report on the enhancement of the electrocatalytic activity of PtPb ordered intermetallic compounds towards MeOH and EtOH oxidation in alkaline aqueous solutions. To achieve this, carbon black (CB)-supported Pt₃Pb(core)–PtPb(shell) intermetallic NPs (Pt₃Pb–PtPb NPs/CB) were synthesized via a method (hereafter referred to as the “converting reaction method”) in which the CB-supported Pt NPs react with a Pb precursor in the presence of a reducing agent under microwave irradiation. In the converting reaction method, the Pb atoms were only observed in the PtPb NPs and not on the CB surfaces. In other words, Pb NPs were not formed on CB in the reaction with microwaves, indicating the selective reaction of Pb atoms with Pt NPs on the CB surfaces, as previously reported by Bauer and our group [13,14]. By controlling the amount of Pb atoms, the core–shell structure with Pt₃Pb and PtPb intermetallic phases can be formed in a NP. The activities of Pt₃Pb–PtPb NPs/CB were compared with those of the reference samples consisting of pure PtPb NPs/CB and Pt₃Pb NPs/CB, which were prepared on the CB through the co-reduction reaction of the Pt and Pb precursors in the presence of a reducing agent and CB (hereafter referred to as the “co-reduction reaction method”). As mentioned above, previously, we have reported that PtPb and PtBi ordered intermetallic phases are the most promising electrocatalysts for MeOH and EtOH oxidations via the exhaustive screening of the ordered intermetallic phases for alkaline MeOH and EtOH oxidations [12]. Yang also reported promising electrocatalytic activity of PtBi towards alkaline MeOH oxidation, which is comparable to our results for the MeOH oxidation observed on pure PtBi and PtPb NPs [15]. In addition, several Pd-based alloys have also been examined towards the EtOH oxidation in an alkaline environment [16–18]. Among Pd-based alloys, Pd alloyed with Ni (PdNi) [16] demonstrated the highest alkaline EtOH oxidation activity and the activity is comparable with that of the pure PtPb NPs. In this research, our current results obtained with Pt₃Pb–PtPb NPs/CB were compared with that of works mentioned above.

2. Experimental section

2.1. Materials

The following chemicals were used to synthesize the NPs: dichloro(1,5-cyclooctadiene)platinum(II) (Pt(COD)Cl₂) (99.9%, Aldrich), (CH₃COO)₂Pb·3H₂O (99%, Wako), ethylene glycol (99.5%, Kanto Chemical) and Vulcan carbon black (CB, XC-72R, E-TEK).

For the electrochemical experiments, sulphuric acid (H₂SO₄, 99.999%, Aldrich), potassium hydroxide (KOH, 85%, Wako), formic acid (FA, 88% analytical reagent, Mallinckrodt), isopropyl alcohol (99.7%, Wako), methanol (MeOH, 99%, Wako), ethanol (EtOH, 99%,

Wako) and Nafion solution (Aldrich, wt. 5 % in water/aliphatic alcohols, 1100 EW) were used as received.

2.2. Synthesis of pure PtPb NPs using the co-reduction reaction method

Pt(COD)Cl₂ (0.0151 mmol), (CH₃COO)₂Pb·3H₂O (0.0227 mmol) and Vulcan CB (0.020 g) were dissolved in 50 mL of ethylene glycol. Then, 0.04 mmol potassium hydroxide was added to the mixture. The mixture was sonicated in a bath-type ultrasonicator and treated in a flask with a reflux apparatus for 6 min under 300 W microwave radiation. The mixture in the flask was then cooled to room temperature with water and treated again under microwave (focused microwave instrument, CEM) radiation of 300 W for 6 min. After the mixture cooled, the PtPb NPs/CB were collected via centrifugation, washed sequentially with EtOH and water, and finally dried under vacuum.

2.3. Synthesis of Pt₃Pb(core)–PtPb(shell) NPs using the converting reaction method

Pt(COD)Cl₂ (0.0151 mmol), (CH₃COO)₂Pb·3H₂O (0.0076 mmol) and Vulcan CB (0.020 g) were dissolved in 50 mL of ethylene glycol. Then, 0.04 mmol potassium hydroxide was added to the mixture. The mixture was sonicated in a bath-type ultrasonicator and treated in a flask with a reflux apparatus for 6 min under 300 W microwave radiation. The mixture in the flask was then cooled to room temperature with water and treated again under microwave (focused microwave instrument, CEM) radiation of 300 W for 6 min. After the mixture cooled, the PtPb NPs/CB was collected via centrifugation, washed sequentially with EtOH and water, and finally dried under vacuum.

2.4. Synthesis of bulk ordered intermetallic PtPb

Polycrystalline bulk samples of intermetallic PtPb were synthesized using an arc furnace in a pure Ar atmosphere (99.9999%) as a reference for the hard X-ray photoemission spectroscopy (HXPES) measurements. All of the starting materials were purchased from Furuya Kinzoku Co. Stoichiometric quantities of Pt (99.9%) and Pb (99.999%) were melted together in a pure Ar (99.9999%) atmosphere at 2000 °C or higher for 24 h and subsequently cooled to room temperature. *p*XRD analysis confirmed that the bulk PtPb exists as a pure hexagonal phase of space group *P*6₃/*mmc*.

2.5. Preparation of pure Pt₃Pb NPs/CB

Carbon supported Pt₃Pb was prepared by wet-chemical approach using NaBH₄ as a reducing agent. In the synthesis, H₂PtCl₆·6H₂O (0.062 mmol), Pb(NO₃)₂ (0.027 mmol) and CB (60 mg) were dissolved in anhydrous methanol and transferred to a double neck round bottom flask without exposing into air. 6 mmol of NaBH₄ was dissolved in anhydrous methanol and then injected to the precursor solutions under Ar-atmosphere. The solutions were stirred for 15 h to complete the reaction under Ar-atmosphere. The black colour suspensions were centrifuged for 10 min at 2000 rpm to yield a black colour precipitate and then subsequently washed with 20 mL of anhydrous methanol for three times and dried under vacuum. The sample obtained was heat treated for 2 h at 600 °C in Ar.

2.6. Characterization of the synthesized NPs

Powder X-ray diffraction (*p*XRD) was performed using CuK α radiation (Panalytical X'Pert PRO; λ = 0.1548 nm) with an

increment of 0.02° in a range of diffraction angles from 20 to 80° . An obliquely cut Si crystal (non-reflection Si plate) was used as a sample holder to minimize the background. HX-PES was performed using X-rays with a photon energy of 5.95 keV at BL15XU of SPring-8, Japan. Sample powders were first dispersed in EtOH and dropped onto carbon substrates. The sample was thoroughly dried in air and transferred into an ultra-high-vacuum (UHV) chamber equipped with an electron spectrometer (Vacuum Generator, Scienta R4000). The binding energy of the photoelectrons was referenced to the Fermi energy of a Au film that was electrically contacted to the sample. Transmission electron microscopy (TEM/STEM) images were obtained with a JEOL 2100-F microscope with an operating voltage of 200 kV. The composition of the PtPb NPs/CB was analyzed by an energy-dispersion spectroscopic (EDS, Oxford link system) analyzer, which was coupled to the TEM. The sample for TEM was prepared by dropping a MeOH suspension of the sample powder onto a copper microgrid. The sample was thoroughly dried in vacuum prior to the observation. The chemical composition of the CB-supported NPs was determined using inductively coupled plasma-mass spectrometry (ICP-MS, PE-3300 DV, Perkin Elmer).

2.7. Preparation of PtPb NPs/CB- and Pt NPs/CB-coated GC electrodes and their electrochemistry

A suspension of the PtPb or Pt NP/CB ink was prepared by mixing 4 mg of the dried NP/CB sample, 3.98 mL of water, 1 mL of isopropyl alcohol, and 20 μ L of 5% w/w Nafion solution. The mixture was then sonicated in a bath-type ultrasonicator for 15 min. 6 μ L of each NP suspension was loaded onto a glassy carbon (GC) electrode with a diameter of 5 mm. The loading weight (0.96 μ g cm^{-2} of Pt NPs) on the GC electrode surface was maintained throughout the experiments. A conventional electrochemical setup was used to evaluate the efficiency of the NPs towards the oxidations of FA, MeOH, and EtOH under an Ar atmosphere. The NP-coated GC electrode, a platinum wire, and an Ag/AgCl (NaCl 3 M) electrode (0.209 V vs. NHE) were used as the working, auxiliary, and reference electrodes, respectively. The NP-coated GC electrodes were rotated to remove bubbles from the electrode surface that likely formed during the oxidation reactions. Pt–Ru alloy NPs and Pd NPs (on a Vulcan XC-72R, E-TEK) were used as reference samples for MeOH and EtOH oxidations.

CO stripping voltammograms were obtained in 0.1 M KOH or H_2SO_4 solutions. In these experiments, NP-coated GC electrodes were prepared under identical conditions. In the first experiment, 0.1 M KOH or H_2SO_4 solutions were purged with Ar gas for 30 min, after which high-purity CO (99.9%) was injected (note that CO should only be used in a well-ventilated hood) into the solutions for 30 min while maintaining the electrode potential at the initial open-circuit potential. The dissolved CO was subsequently removed from the solution by bubbling through nitrogen gas for 30 min while maintaining the applied electrode potential. Finally, the CO stripping voltammograms were obtained via positive scanning from the applied electrode potential at scan rate of 10 mV s^{-1} in N_2 -saturated 0.1 M KOH or H_2SO_4 solutions.

3. Results and discussion

Fig. 1 shows the *p*XRD profiles for the (a) CB, (b) Pt NPs/CB, (c) converting reaction-synthesized PtPb NPs/CB and (d) co-reduction reaction-synthesized PtPb NPs/CB. Simulated *p*XRD patterns for the Pt phase (face-centred cubic (fcc), *Fm*- $3m$, $a = 0.3925$ nm), PtPb (hexagonal, *P63/mmc*, $a = b = 0.426$ nm, $c = 0.548$ nm), and Pt₃Pb ordered intermetallic phases (Cu_3Au , *Pm*- $3m$, $a = b = c = 0.393$ nm) are indicated by the solid bars in the bottom portion of the figure. All of the *p*XRD profiles in Fig. 1 exhibit two peaks at 25.0° and 43.5°

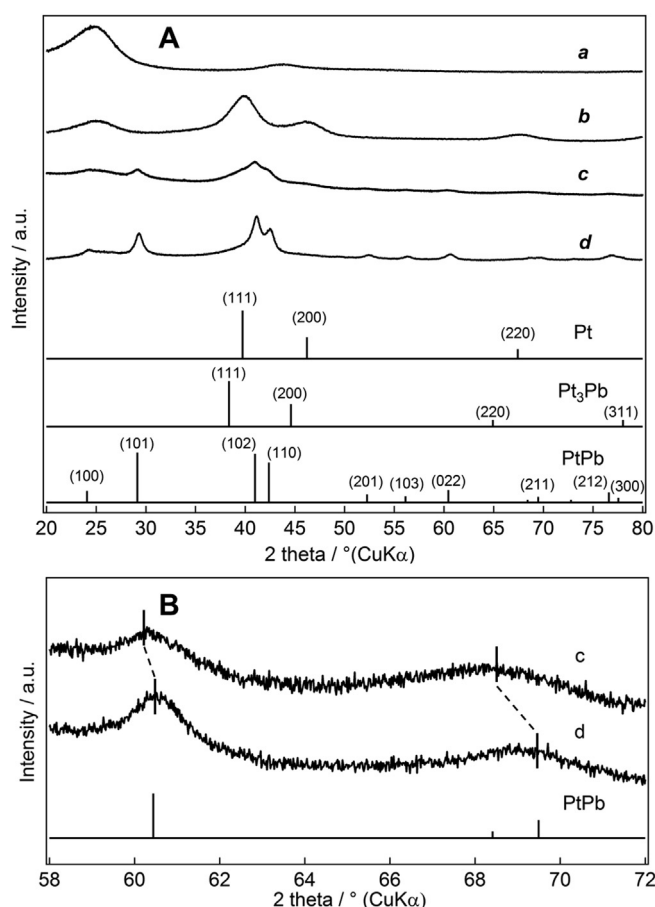


Fig. 1. (A) *p*XRD patterns of CB (a), Pt NPs/CB used as a starting material (b), converting reaction- (c) and conventional reaction-synthesized PtPb NPs/CB (d). The solid bars in the bottom half of the figure are the simulated *p*XRD peaks for the Pt and the ordered intermetallic PtPb and Pt₃Pb phases. (B) *p*XRD patterns of samples (c) and (d) from 58° to 72° .

that correspond to the (0 0 2) and (1 0 1) reflections of carbon (trace a), respectively. The *p*XRD profile of Pt NPs/CB (trace b) reveals peaks at 39.8° , 45.3° and 67.5° , corresponding to the (1 1 1), (2 0 0), and (2 2 0) reflections, respectively, of an fcc-type structure (*Fm*- $3m$, $a = 0.393$ nm) similar to that of pure Pt (*Fm*- $3m$, $a = 0.3925$ nm), as indicated in the simulated *p*XRD peaks. The profiles of the samples obtained through the converting reaction and co-reduction reaction (traces c and d) show peak patterns that can be indexed to the hexagonal-type structure of PtPb ordered intermetallic structure. This includes the characteristic peaks for the PtPb ordered intermetallic phase, which distinguish the PtPb ordered intermetallic phase from the Pt fcc structure. These peaks can be observed from 50 to 80° in both traces (c) and (d). The NPs prepared via the converting reaction also exhibit small peaks for the Pt₃Pb (1 1 1) and (2 0 0) phases at 38.4° and 44.6° , respectively, indicating the coexistence of PtPb and Pt₃Pb phases in the NPs. It is evident from the data that the Pt₃Pb phase was also formed in the NPs by a wet-chemical approach. Peak shifts for the PtPb (0 2 2) and (2 1 1) phases to smaller angles were observed in the region from 58 to 72° for the NPs prepared via the converting reaction (Fig. 1B), resulting in an increase in the lattice parameter of the (0 2 2) and (2 1 1) phases. The shift of the (2 1 1) peak is 1.2° . The PtPb NPs (trace d) prepared by the co-reduction reaction do not exhibit peaks apart from those assigned to the PtPb ordered intermetallic phase, respectively, nor do they exhibit any peak shifts. These results confirmed the formation of pure PtPb ordered intermetallic NPs

produced by the co-reduction reaction to be used as reference samples for the electrocatalytic activity tests.

Fig. 2 displays the HX-PES profiles in the Pt 4f region for PtPb NPs prepared with (a) the converting reaction and (b) the co-reduction reaction as well as the bulk references (c) PtPb and (d) Pt. The Pt 4f peak for the bulk PtPb was shifted 0.3 eV towards higher binding energies relative to the corresponding peak for the bulk Pt. The Pt 4f peaks for the NPs/CB prepared via the converting reaction and co-reduction reaction were consistent with those of the bulk PtPb, indicating that the chemical composition and atomic environment of the NP surfaces prepared via either of the two methods were identical to those of the bulk PtPb. Therefore, we conclude that the surfaces of the NPs prepared via the converting and co-reduction reactions consist of a PtPb ordered intermetallic phase.

Figs. 3 and 4(A) and (B) show the TEM images obtained with commercially available Pt NPs/CB and (A) co-reduction- and (B) converting reaction-synthesized NPs/CB. Pt and PtPb NPs appeared as dark spots that were uniformly dispersed on the CB. The distributions of the size of the Pt and PtPb NPs were evaluated using approximately 100 particles in the TEM images. The average diameters of the Pt NPs and the co-reduction- and converting reaction-synthesized PtPb NPs were calculated as 2.5, 3.0, and 4.6 nm, respectively, and they exhibited a narrow particle-size distribution. We also calculated the theoretical diameter of hemispherical PtPb ordered intermetallic compound NPs to be 3.0 nm on the basis of the density (15.51 g cm^{-3}) [19] of the PtPb ordered intermetallic compound. The hemispherical Pt NPs with a diameter of 2.5 nm were reacted with Pb^{2+} to prepare the PtPb ordered intermetallic compound. The particle size increased to the theoretical value when the PtPb ordered intermetallic compounds were formed on CB, as shown in Fig. 4B. In addition, from a comparison of the TEM image of the converting reaction-synthesized PtPb NPs/CB with that of Pt NPs/CB used as a starting material for the converting reaction, it can be observed that the degree of spatial dispersity of the Pt NPs on the CB is retained on the NPs/CB prepared via the

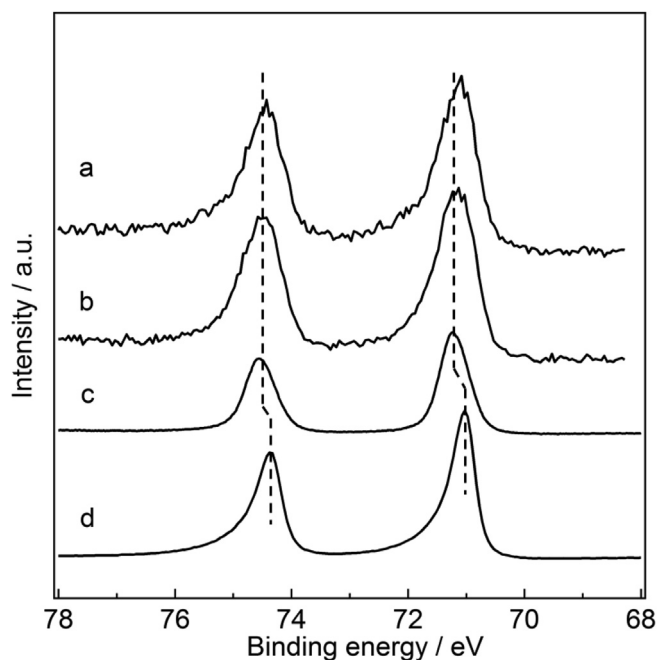


Fig. 2. HX-PES profiles in the Pt 4f region for PtPb NPs/CB prepared via (a) the converting reaction method and (b) conventional synthesis. The HX-PES spectra obtained with (c) ordered intermetallic bulk phase PtPb and (d) bulk Pt are shown as references.

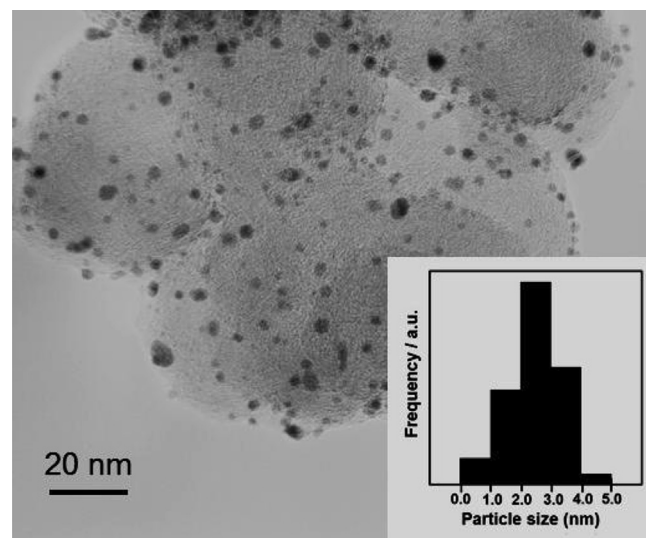


Fig. 3. Low-resolution TEM image of commercially available 20 wt% Pt NPs/CB and its particle size distribution histograms.

converting reaction due to the conversion of nanocrystalline Pt metals to the PtPb intermetallic compound.

Fig. 5 shows low-resolution (LR) and high-resolution (HR) TEM images of Pt₃Pb NPs prepared with the co-reduction reaction, and compositional mapping of Pt and Pb atoms. The average diameters of the Pt₃Pb NPs prepared with the co-reduction reaction were calculated as 4.2 nm. The particle-size distribution is similar to those observed with PtPb and Pt NPs/CB. The HR-TEM image (Fig. 5B) and FFT patterns (inset of Fig. 5C) of the Pt₃Pb NPs prepared using the co-reduction reaction indicate that the NPs are single crystalline. The *d* lattice spacings of the NPs presented in the HR-TEM image are 0.233 and 0.190 nm, which closely match those of the (1 1 1) and (2 0 0) planes, respectively, for Pt₃Pb ordered intermetallic compounds (0.233 nm for the (1 1 1) plane and 0.190 nm for the (2 0 0) plane). STEM–energy dispersive spectroscopy (EDS) mappings also demonstrated that the average mole ratios of Pt to Pb for Pt₃Pb NPs prepared with the co-reduction reaction were consistent with the desired value for Pt₃Pb, namely, Pt:Pb = 80.3:19.7.

Fig. 6A and B displays HR-TEM images of the NPs prepared via the co-reduction and converting reactions, respectively, and the corresponding fast Fourier-transform (FFT) patterns obtained from the selected areas are denoted by the dotted squares. The HR-TEM image and FFT patterns of the NPs prepared using the co-reduction reaction indicate that the NPs are single crystalline. The *d* lattice spacings of the NPs presented in the HR-TEM image are 0.215 and 0.218 nm, which closely match those of the (2 2 0) and (2 0 0) planes, respectively, for PtPb ordered intermetallic compounds (0.216 nm for the (2 2 0) plane, 0.218 nm for the (2 0 0) plane). On the other hand, the HR-TEM image of the NPs prepared via the converting reaction exhibits two crystalline phases in the parts of core and shell of the NPs. The *d* lattice spacings (0.336 and 0.227 nm) in the core and shell differ from that of the (1 0 0) planes of the Pt₃Pb ordered intermetallic phase (0.406 nm) and the (2 0 0) planes of the PtPb ordered intermetallic phase (0.218 nm), indicating an expansion and contraction of the *d* lattice spacings in the PtPb shell and Pt₃Pb core. The two FFT images shown in Fig. 6B collected from the core and shell demonstrate that the Pt and Pb atoms were arranged in crystal structures corresponding to structurally modified Pt₃Pb and PtPb ordered intermetallic phases. Fig. 6C and D displays the profiles of the EDS line scans along with

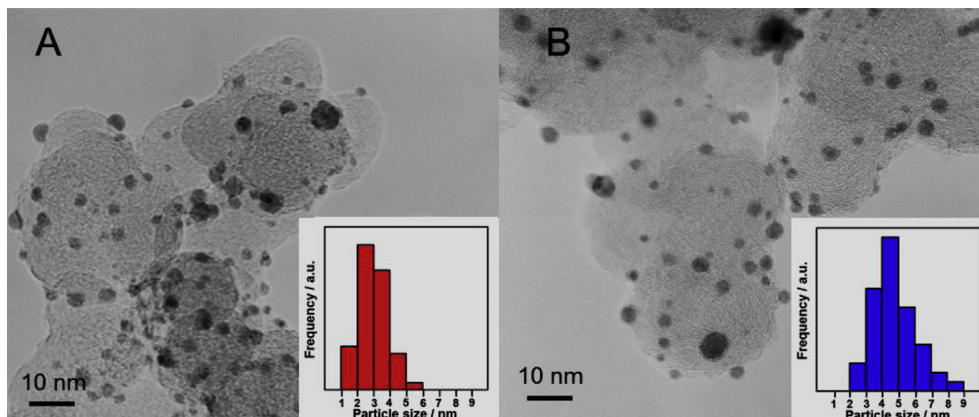


Fig. 4. TEM images of NPs prepared via (A) the co-reduction and (B) the converting reaction synthesis and their particle size distribution histograms.

the lines presented in the insets of figure depicting the two NPs prepared using the co-reduction and converting reaction. When compared with the two line profiles, a Pt-rich core for Pt_3Pb can be clearly observed in the shadowed regions of Fig. 6D. The average mole ratios of Pt to Pb, which were evaluated with STEM–EDS mappings, were consistent with the desired value for PtPb , $\text{Pt:Pb} = 53.0 \pm 3:47.0 \pm 3$ on any point on the PtPb NPs prepared with the co-reduction reaction. The average mole ratios of Pt to Pb in the PtPb NPs prepared with the converting reaction were $\text{Pt:Pb} = 70.5:29.5$ in the centre of the NPs, as shown in Fig. 6B, and $\text{Pt:Pb} = 54.2:45.8$ on the surface of the NPs. These *p*XRD, HX-PES, TEM/STEM results suggest the formation of Pt_3Pb – PtPb intermetallic compound core–shell NPs, pure PtPb and Pt_3Pb NPs synthesized from the converting reaction and co-reduction reaction methods, respectively. The formation of the Pt_3Pb phase as a core in NPs during the converting reaction can be easily understood by

considering the crystal structure of Pt and Pt_3Pb ordered intermetallic phases. When Pb atoms are formed by the reduction of Pb ions with reducing agents because a small amount of Pb atoms react with an absolutely large amount of Pt atoms in the early stage of the reaction, Pb atoms enter into the fcc type structure of Pt NPs. The stable crystal structure that will be formed in the NPs as a result of Pb atoms entering into Pt NPs might be an ordered intermetallic Pt_3Pb phase having the structure type of Cu_3Au . As the reaction proceeds, the ratio of Pb atoms in the NPs surface gradually increases and the surface structure becomes the hexagonal $P63/mmc$ structure of the PtPb ordered intermetallic phase. The core–shell structure composed of Pt_3Pb and PtPt ordered intermetallic phases can be formed by optimizing the composition of the reaction solution containing a Pb precursor, Pt NPs/CB powder, and a reducing agent as well as the reaction temperature and time and the power of the microwave. Naturally, when the rate of Pb reduction is higher

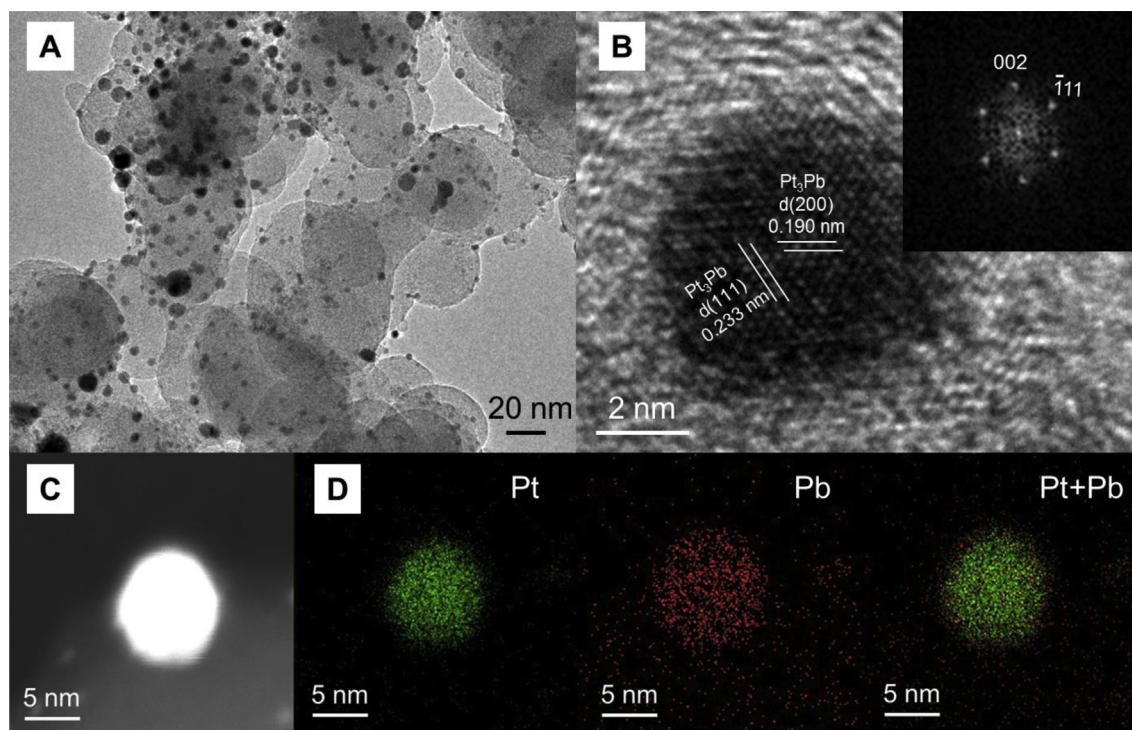


Fig. 5. (A) Low-resolution and (B) high-resolution TEM and (C) STEM and (D) STEM-EDS mapping profile images of CB-supported Pt_3Pb NPs. Inset: FFT pattern obtained from image B.

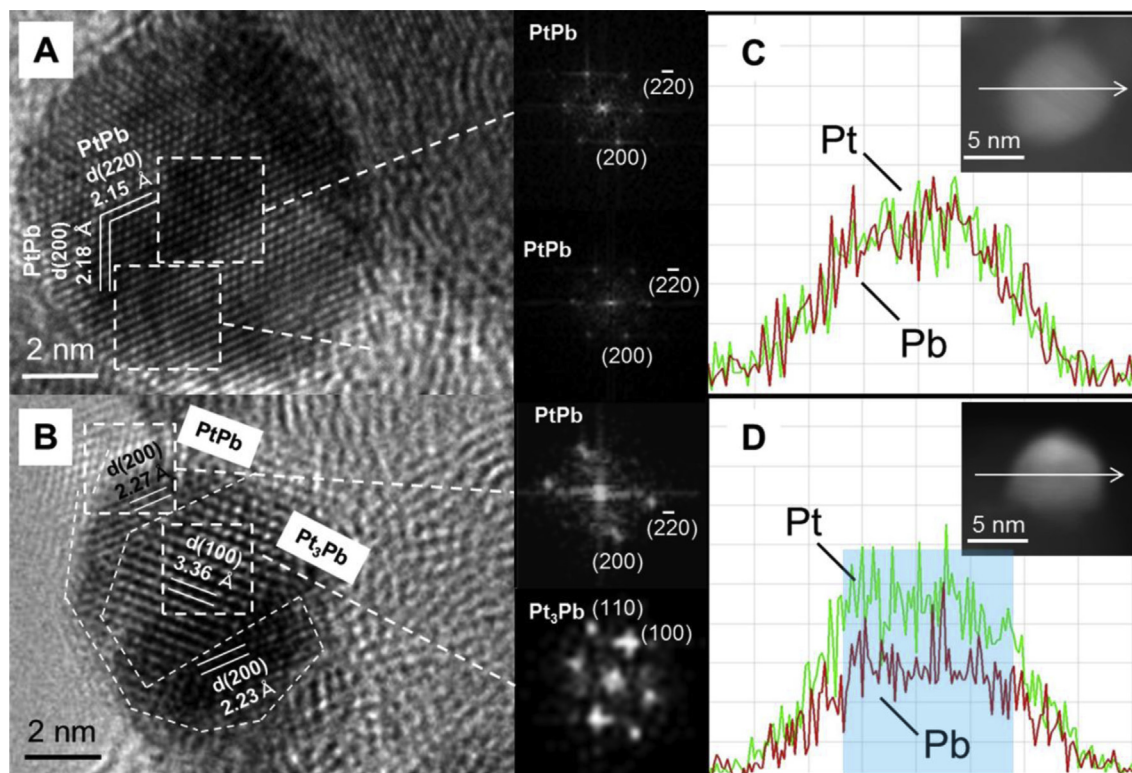


Fig. 6. (A, B) HR-TEM images and (C, D) EDS Pt (green line) and Pb (red line) line profiles of the NPs prepared via (A, C) the co-reduction reaction and (B, D) the converting reaction. The FFT images in (A, B) were collected from the selected areas denoted by the dotted square (For interpretation of the references to color in this figure legend, the reader is referred to the web version of this article.).

than the diffusion rate of Pb atoms into the Pt NPs, the Pb layer is formed on the surface of Pt NPs. It is important to consider the balance of the reduction rate of Pb ions on the NP surfaces and the diffusion rate of Pb atoms into the NPs. The core–shell structure of Pt₃Pb and PtPb ordered intermetallic phases, which were prepared with care and over several trials to find the appropriate conditions, was examined to enhance the electrocatalytic activities of MeOH and EtOH oxidations. ICP-MS measurements revealed that the weight percentages of Pt in PtPb NPs/CB, Pt₃Pb NPs/CB, and Pt₃Pb–PtPb NPs/CB were 12.8, 18.3, and 20.0 wt%, respectively.

Fig. 7A represents the linear sweep voltammograms (LSVs) for the FA oxidation on Pt NPs/CB-, pure PtPb NPs/CB-, intermetallic Pt₃Pb–PtPb core–shell NPs/CB-, and pure Pt₃Pb NPs/CB-immobilized glassy carbon (GC) electrodes in a 0.5 M FA aqueous solution containing 0.1 M H₂SO₄. The oxidation currents were normalized to the weight of the Pt atoms immobilized on the GC electrodes and are presented as the mass activity (MA) in mA μg^{−1}. The Pt₃Pb NPs/CB exhibited the highest mass activity towards FA oxidation in acidic media among the four examined NPs/CB samples. The FA oxidation activities can be ranked as: Pt NPs/CB < Pt₃Pb–PtPb NPs/CB < pure PtPb NPs/CB < Pt₃Pb NPs/CB. Murray et al. have reported the electrocatalytic activity for FA oxidation on Pt₃Pb NPs (average particle size: 3.7 nm)/CB in 0.5 M FA and 0.1 M H₂SO₄ at a potential scan rate of 20 mV s^{−1} and found that the mass activity at 0.3 V (vs. NHE) was 0.375 mA μg_{Pt}^{−1}. Our pure Pt₃Pb NPs exhibited a higher mass activity (0.52 mA μg_{Pt}^{−1} at 0.3 V (vs. NHE)) than one reported by Murray et al. in the FA oxidation [20]. Therefore, our higher activity Pt₃Pb NPs were used to compare the electrocatalytic activities for MeOH and EtOH oxidation in alkaline media. In addition, Guo et al. synthesized Pt(core)–PtPb(shell) NPs on CB with a two-step microwave-assisted polyol process, such as the process that we used to prepare

Pt₃Pb–PtPb NPs, and reported that the Pt–PtPb NPs exhibited enhanced catalytic activity (0.78 mA μg_{Pt}^{−1} at 0.3 V vs. NHE) and durability for FA oxidation. Our Pt₃Pb–PtPb NPs (0.20 mA μg_{Pt}^{−1} at 0.3 V vs. NHE) are far lower than their Pt–PtPb NPs in terms of their activity for FA oxidation [21]. However, the alkaline MeOH (Fig. 7B) and EtOH (Fig. 7C) oxidations on pure PtPb, pure Pt₃Pb, and intermetallic Pt₃Pb–PtPb core–shell NPs exhibited different properties: the surfaces of the intermetallic Pt₃Pb–PtPb core–shell NPs largely enhance the MeOH and EtOH oxidations. In particular, the EtOH oxidation current substantially exceeded the MeOH oxidation current. Commercially available CB-supported Pt–Ru alloy and Pd catalysts that have been recognized as anode catalysts [22–24] were also tested in the MeOH and EtOH oxidations in alkaline solutions for comparison. The oxidation activities of the Pt–Ru alloy and Pd NPs/CB are clearly lower than those of the Pt₃Pb–PtPb NPs/CB. As shown in Fig. 4, the average particle sizes of the NPs are significantly different from those produced by co-reduction and those produced by the converting reaction, with the former being smaller. The difference in the surface areas of the NPs exposed to the test solutions should also be taken into account for the comparison of their catalytic activity. The comparison of catalytic activities should be evaluated with NPs that have the same surface areas or should be compared using specific activities calculated with surface areas. However, as observed in the results of Fig. 4, the converting reaction-synthesized Pt₃Pb–PtPb NPs that have a smaller surface area (and larger particle size) exhibit higher catalytic activity. This difference in activity between NPs prepared with the co-reduction and converting reactions clearly indicates that if the specific catalytic activities were calculated with the surface areas of the NPs, a much larger difference in the catalytic activity will be evaluated between pure PtPb and Pt₃Pb–PtPb NPs. The Pt₃Pb–PtPb NPs will exhibit higher activities than that of pure PtPb

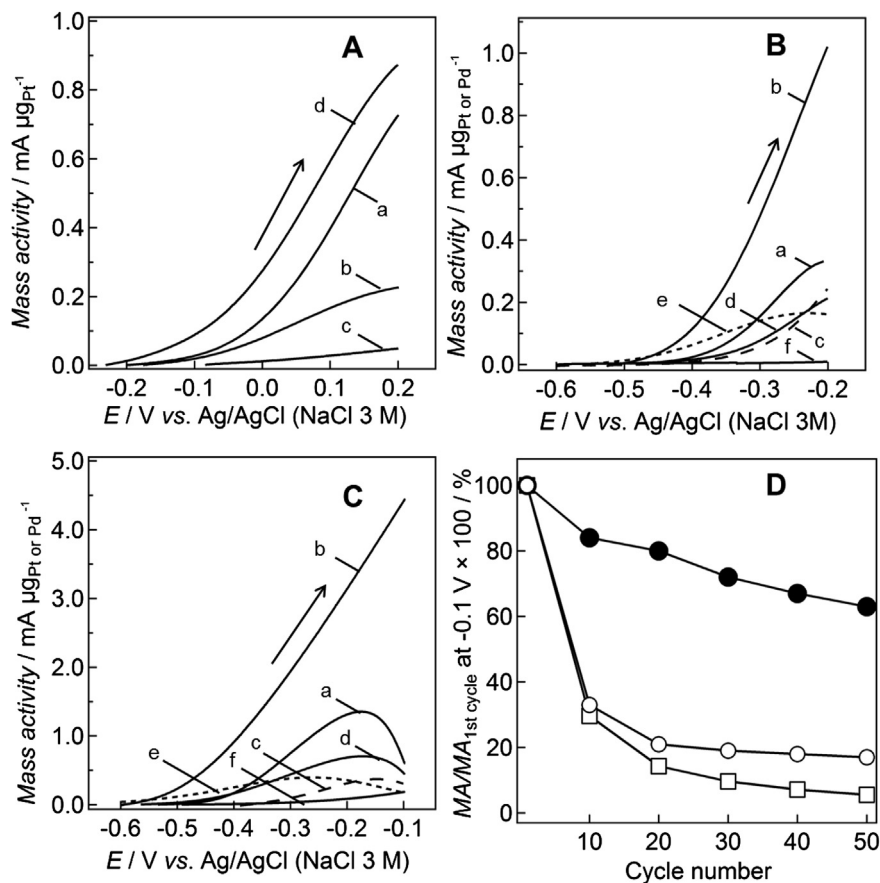


Fig. 7. LSVs obtained in (A) 0.5 M FA + 0.1 M H_2SO_4 , (B) 0.5 M MeOH + 0.1 M KOH, and (C) 0.5 M EtOH + 0.1 M KOH aqueous solutions with (a) co-reduction reaction-synthesized PtPb NPs/CB, (b) converting reaction-synthesized PtPb NPs/CB, (c) Pt NPs/CB, (d) Pt_3Pb NPs/CB, (e) Pt–Ru alloy NPs/CB and (f) Pd NPs/CB-fixed GC electrodes at a scan rate of 10 mV s^{-1} and an electrode rotation speed of 2000 rpm. Panel D represents the dependences of the oxidative mass activity (MA) at -0.1 V (vs. Ag/AgCl (3 M NaCl)) on the cycle number with Pt NPs/CB (\circ), Pt_3Pb –PtPb NPs/CB (\bullet) and pure PtPb NPs/CB (\square).

NPs. As a result of the comparison of our current results with work mentioned above, it can be concluded that Pt_3Pb –PtPb intermetallic core–shell NPs show much higher electrocatalytic activity towards MeOH and EtOH, especially in EtOH oxidation than that of the previously reported results [12,15,16]. Long-term durability of the electrocatalytic activity is critical for real fuel cell applications. The long-term activity and stability of Pt, pure PtPb and Pt_3Pb –PtPb NPs/CB were examined using cyclic voltammetry (CV) with regard

to the EtOH oxidation reaction. The CVs for pure PtPb and Pt_3Pb –PtPb NPs recorded during 10 cycles are shown in Fig. 8. The changes in oxidation current at the Pt NPs, pure PtPb, and Pt_3Pb –PtPb fixed GC electrodes, monitored at -0.1 V for 50 cycles with a rotation rate of 2000 rpm, are summarized in Fig. 7D. For the Pt NPs- (open circles) and pure PtPb NPs-fixed (open squares) electrodes, the oxidation currents dropped during the first several cycles for the EtOH oxidation. The Pt_3Pb –PtPb NPs prepared via the

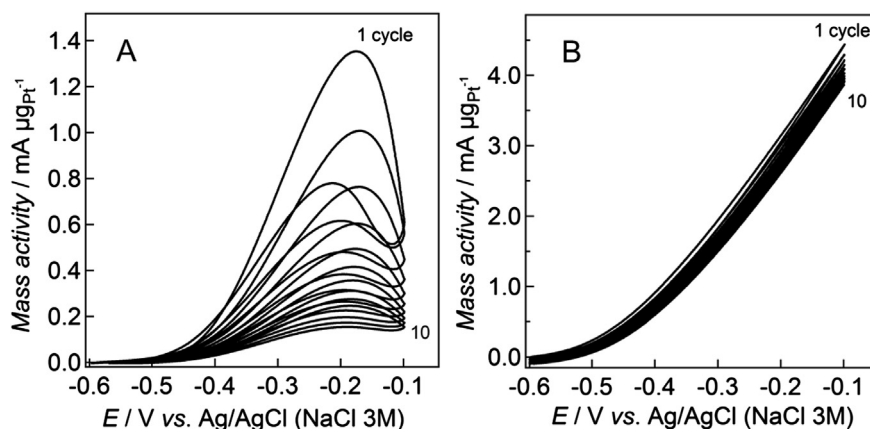


Fig. 8. Cyclic voltammograms for EtOH oxidation with NPs/CB prepared using (A) the co-reduction and (B) the converting reactions in a N_2 -saturated 0.5 M EtOH + 0.1 M KOH aqueous solution at 2000 rpm and 10 mV s^{-1} .

converting reaction method maintained relatively stable oxidation currents of approximately 60% for 50 cycles (solid circles). Accumulation of the intermediate species adsorbed on the Pt sites during the EtOH oxidation results in the currents drop quickly with potential cycling. The surface of Pt₃Pb–PtPb intermetallic core–shell NPs has the catalytic activity to release the Pt active sites for further adsorption of reaction species. In contrast, in the pure PtPb surface, the intermediate species are accumulated on the Pt atoms because its surface does not have ability to remove the intermediate species from the Pt atoms. The origin of the ability to remove the intermediate species will be discussed with the reaction mechanism for EtOH oxidation.

To make clear the difference in the surface structure between pure PtPb and Pt₃Pb–PtPb NPs, CO poisoning tests were performed with Pt₃Pb–PtPb and pure PtPb NPs. Fig. 9 presents the CO stripping voltammograms with Pt NPs/CB, pure PtPb NPs/CB, and Pt₃Pb–PtPb intermetallic core–shell NPs/CB in acidic media. The voltammogram obtained with Pt NPs (Fig. 9A) shows a sharp oxidation stripping peak caused by the oxidation of CO molecules adsorbed on the Pt surfaces at -0.59 V (vs. Ag/AgCl 3 M). The CO stripping CV peak from the Pt₃Pb–PtPb NPs is shifted towards higher potential compared with that of the Pt NPs but to lower potentials when compared to that observed for pure PtPb NPs. The decrease in the charge for the oxidation of adsorbed CO molecules can also be observed with the shift of the stripping peak. Because the charge for the oxidative CO stripping is a measure of the CO tolerance on the NP surface, the decrease in the charge for the oxidative CO stripping on the PtPb and Pt₃Pb–PtPb NPs indicates that the PtPb and Pt₃Pb–PtPb NPs still have a higher CO tolerance than the Pt NPs. Therefore, the order of the FA oxidation activity shown in Fig. 7A is consistent with the degree of the shift of the CO stripping peak. Additionally, in alkaline aqueous solutions, pure PtPb and Pt₃Pb–PtPb NPs exhibited a smaller charge for the CO stripping when compared with Pt NPs. The charge for the oxidation of adsorbed CO on the NP surfaces is the smallest in the Pt₃Pb–PtPb NP surface (Fig. 10). From these CO stripping data, it can be confirmed that the surface structure of Pt, pure PtPb and Pt₃Pb–PtPb NPs is significantly different from each other. The dramatic drop in the quantity of CO adsorbed onto the Pt₃Pb–PtPb intermetallic compound core–shell NP surface is considered to be caused at least in part by a direct consequence of its structure, specifically, the difference between the Pt–Pt distance in pure PtPb and modified PtPb on the Pt₃Pb–PtPb intermetallic core–shell NPs. The increase in the lattice parameters for the (2 0 0) planes of the

PtPb shell may prevent the CO from binding to the bridge or three-fold hollow site configurations on the modified PtPb phase in Pt₃Pb–PtPb intermetallic compound core–shell NPs.

As is well known, Pt is the most widely used anode catalyst. However, pure Pt is not efficient catalyst for alcohol oxidation and Pt-based bimetallic alloys with Ru, Rh, Ir, Sn and Sb have been investigated extensively [25–30]. For example, Jin et al. have discussed potential-dependent phase diagrams for surface oxidants of OH_{ads} formation on Pt(1 1 1), Pt(2 1 1) and Sn adatom-modified Pt(1 1 1) and Pt(2 1 1) surfaces for the EtOH oxidation, which have been determined using density functional theory (DFT) calculations and considered that in the presence of Sn, both the OH_{ad} formation and C–C dissociation are more difficult on the Pt(2 1 1) surface, whereas the acetic acid formation is more facile over both Pt(2 1 1) and Pt(1 1 1) surfaces, shifting the production selectivity towards acetic acid. It was concluded that the large increase in the rate observed in their experiment is associated with both the decrease in the activation barriers of C–C dissolution as well as the increased concentration of surface OH_{ads} at low potential on the Pt(1 1 1) surfaces due to the presence of Sn [25]. They calculated the onset potentials of OH_{ad} formation on Pt(1 1 1) and Sn modified Pt(1 1 1) surfaces. Sn modified Pt(1 1 1) surface shifted the onset potential of OH_{ad} formation from 0.59 V (on Pt sites) to 0.23 V (on PtSn sites), indicating that the modification of Pt by Sn can provide OH[−] adsorption sites at low potentials. Sheng et al. have also found using DFT calculations in the models of transition metals (Ru, Rh, Pd, Os and Ir) alloyed on the top layer of Pt(1 1 1) that the active metals increase the activity of β -dehydrogenation of EtOH but lower the OH_{ad}

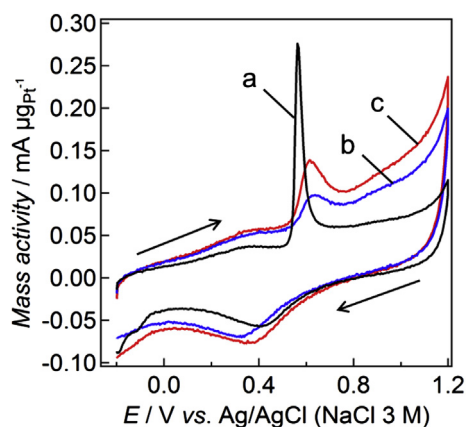


Fig. 9. CO-stripping voltammograms obtained using commercial (a) Pt NPs/CB, (b) pure PtPb NPs/CB, and (c) Pt₃Pb–PtPb NPs/CB in Ar-saturated 0.1 M H₂SO₄ aqueous solution at 2000 rpm and 10 mV s^{−1}.

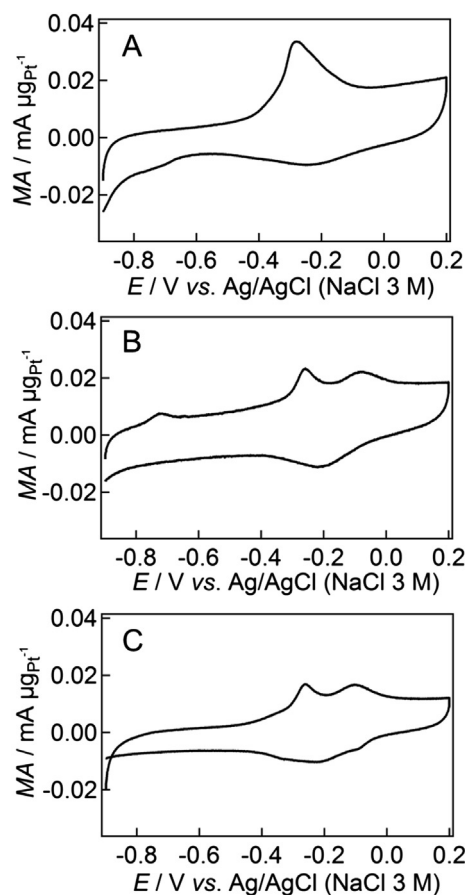
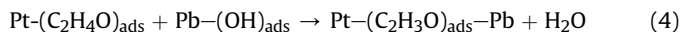
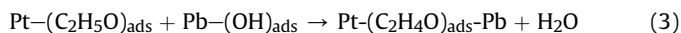


Fig. 10. CO-stripping voltammograms obtained using commercial (a) Pt NPs/CB, (b) pure PtPb NPs/CB, and (c) Pt₃Pb–PtPb NPs/CB in Ar-saturated 0.1 M KOH aqueous solution at 2000 rpm and 10 mV s^{−1}.

formation potential resulting in the active site being deposited with transition metals. By considering both β -dehydrogenation and OH_{ad} formation, the transition metals Ru, Os and Ir are identified to be unsuitable for the promotion of CO_2 selectivity and only Rh is able to increase the selectivity of CO_2 in the EtOH oxidation [31].

The possible EtOH oxidation reaction mechanism in alkaline media might be explained by the following process (Eqs. (1)–(4)) [32,33]. Because the onset potential for CO oxidation on the Pt_3Pb – PtPb intermetallic core–shell NPs is much higher than that for alcohol oxidation, Pt_3Pb – PtPb intermetallic core–shell NP surfaces work more efficiently in the dehydrogenation of the EtOH oxidation. The EtOH dehydrogenation actively continues on the catalyst surface around the onset potential of EtOH oxidation to increase the oxidation current. The OH_{ads} supplied by the solution of OH^- ions are key species that catalyze the EtOH oxidation reaction. OH_{ads} species can be generated on Pb atoms by the discharge of OH^- in alkaline solution. The formation of Pb – OH_{ads} would be accelerated on the surface of the Pt_3Pb – PtPb intermetallic compound core–shell NPs in alkaline media and would contribute to the increase in the oxidation currents of EtOH at lower electrode potential, although some Pt – OH_{ads} species also work in the EtOH oxidation reactions at higher electrode potential. The OH_{ads} species on Pb atoms can react with the intermediate species adsorbed on the Pt sites to release the Pt active sites for further adsorption of reaction species.



It can be considered that Pb atoms in the surface of the Pt_3Pb – PtPb intermetallic compound core–shell NPs associate with both the decrease in the activation barriers of dehydrogenation as well as the increased concentration of surface OH_{ads} at low potential and that the Pb atoms in the Pt_3Pb – PtPb intermetallic compound core–shell NPs work more efficiently in the EtOH dehydrogenation and OH_{ad} formation than other metals.

4. Conclusions

We have successfully synthesized intermetallic Pt_3Pb – PtPb core–shell NPs through a converting reaction in ethylene glycol under microwave irradiation by reacting Pt precursors with Pt NPs to form ordered intermetallic phases of Pt_3Pb and PtPb . The pXRD, HX-PES and TEM/STEM characterizations demonstrated that pure PtPb NPs, pure Pt_3Pb NPs and Pt_3Pb – PtPb intermetallic core–shell NPs could be prepared by conventional co-reduction and converting reaction synthesis methods, respectively, without annealing. The intermetallic Pt_3Pb – PtPb core–shell NPs exhibited higher catalytic activity towards MeOH and EtOH oxidation reactions in an alkaline aqueous solution. The enhanced electrocatalytic activities

and tolerance for CO-poisoning as well as the improved stability of Pt_3Pb – PtPb NPs was validated by comparison with commercial Pt NPs, pure PtPb and Pt_3Pb NPs. The structural modification of the PtPb surface influenced by the Pt_3Pb core on the Pt_3Pb – PtPb NPs produces a considerable improvement of the catalytic performance, such as high and stable oxidation activities of EtOH, which might be due to the enhancement of dehydrogenation of EtOH on Pt atoms and the increase of the concentration of OH_{ad} on Pb atoms.

References

- [1] N.W. Deluca, Y.A. Elabd, J. Polym. Sci., Part B: Polym. Phys. 44 (2006) 2201–2225.
- [2] W. Qian, D.P. Wilkinson, J. Shen, H. Wang, J. Zhang, J. Power Sources 154 (2006) 202–213.
- [3] E. Antolini, J. Power Sources 170 (2007) 1–12.
- [4] A.V. Tripković, K.D. Popović, B.N. Grgur, B. Blizanac, P.N. Ross, N.M. Marković, Electrochim. Acta 47 (2002) 3707–3714.
- [5] J.S. Spendlow, A. Ieckowski, Phys. Chem. Chem. Phys. 9 (2007) 2654–2675.
- [6] A. Verma, S. Basu, J. Power Sources 145 (2005) 282–285.
- [7] F.P. Hu, P.K. Shen, J. Power Sources 173 (2004) 877–881.
- [8] M. Nie, H. Tang, Z. Wei, S.P. Jiang, P.K. Shen, Electrochem. Commun. 9 (2007) 2375–2379.
- [9] E.D. Casado-Rivera, J. Volpe, L. Alden, C. Lind, C. Downie, T. Vázquez-Alvarez, A.C.D. Angelo, F.J. DiSalvo, H.D. Abruña, J. Am. Chem. Soc. 126 (2004) 4043–4049.
- [10] D. Volpe, E.D. Casado-Rivera, L. Alden, C. Lind, K. Hagerdon, C. Downie, C. Korzeniewski, F.J. DiSalvo, H.D. Abruña, J. Electrochem. Soc. 151 (2004) A971–A977.
- [11] F. Matsumoto, C. Roychowdhury, F.J. DiSalvo, H.D. Abruña, J. Electrochem. Soc. 155 (2008) B148–B154.
- [12] F. Matsumoto, Electrochemistry 80 (2012) 132–138.
- [13] J.C. Bauer, X. Chen, Q. Liu, T.-H. Phan, R.E. Schaak, J. Mater. Chem. 18 (2008) 275–282.
- [14] A.J. Jeevagan, T. Gunji, N. Sawano, G. Saravanan, T. Kojima, S. Kaneko, G. Kobayashi, F. Matsumoto, ECS Trans. 58 (2014) 25–31.
- [15] M. Yang, J. Power Sources 229 (2013) 42–47.
- [16] Z. Zhang, L. Xin, K. Sun, W. Li, Int. J. Hydrogen Energy 36 (2011) 12686–12697.
- [17] Z.X. Liang, T.S. Zhao, J.B. Xu, L.D. Zhu, Electrochim. Acta 54 (2009) 2203–2208.
- [18] E. Antolini, Energy Environ. Sci. 2 (2009) 915–931.
- [19] second ed., in: T.B. Massalski (Ed.), Binary Phase Diagrams, Vol. 1, ASM International, Materials Park, OH, 1990.
- [20] Y. Kang, L. Qi, M. Li, R.E. Diaz, D. Su, R.R. Adzic, E. Stach, J. Li, C.B. Murray, ACS Nano 6 (2012) 2818–2825.
- [21] Y. Huang, S. Zheng, X. Lin, L. Su, Y. Guo, Electrochim. Acta 63 (2012) 346–353.
- [22] C. Bianchini, P.K. Shen, Chem. Rev. 109 (2009) 4183–4206.
- [23] V. Bambagioni, C. Bianchini, A. Marchionni, J. Filippi, F. Vizza, J. Teddy, P. Serp, M. Zhiani, J. Power Sources 190 (2009) 241–251.
- [24] R.N. Singh, A. Singh, Anindita, Int. J. Hydrogen Energy 34 (2009) 2052–2057.
- [25] J.-M. Jin, T. Sheng, X. Lin, R. Kavanagh, P. Hamer, P. Hu, C. Hardacre, A.M. Bonastre, J. Sharman, D. Thompsett, W.-F. Lin, Phys. Chem. Chem. Phys. 16 (2014) 9432–9440.
- [26] N. Erini, R. Loukrakpam, V. Petkov, E.A. Baranova, R. Yang, D. Teschner, Y. Huang, S.R. Brankovic, P. Strasser, ACS Catal. 4 (2014) 1859–1867.
- [27] A. Kowal, M. Li, M. Shao, K. Sasaki, M.B. Vukmirovic, J. Zhang, N.S. Marinkovic, P. Liu, A.I. Frenkel, R.R. Adzic, Nat. Mater. 8 (2009) 325–330.
- [28] A.O. Neto, R.R. Dias, M.M. Tusi, M. Linardi, E.V. Spinace, J. Power Sources 166 (2007) 87–91.
- [29] J. Ribeiro, D.M. dos Anjos, K.B. Kokoh, C. Coutanceau, J.-M. Leger, P. Olivi, A.R. de Andrade, G. Tremiliosi-Filho, Electrochim. Acta 52 (2007) 6997–7006.
- [30] J.M.S. Ayoub, A.N. Geraldes, M.M. Tusi, E.V. Spinace, A.O. Neto, Ionics 17 (2011) 559–564.
- [31] T. Sheng, W.-F. Lin, C. Hardacre, P. Hu, Phys. Chem. Chem. Phys. 16 (2014) 13248–13254.
- [32] R. Manoharan, J. Prabhuram, J. Power Sources 96 (2001) 220–225.
- [33] W. Du, K.E. Mackenzie, D.F. Milano, N.A. Deskins, D. Su, X. Teng, ACS Catal. 2 (2012) 287–297.